Metal Phosphides as Potential Thermoelectric Materials

Jan-Hendrik Pöhls,[a] Alireza Faghaninia,[b] Guido Petretto,[c] Umut Aydemir,[d], [e] Francesco Ricci,[c] Guodong Li,[f] Max Wood,[d] Saneyuki Ohno,[d,g] Geoffroy Hautier,[c] G. Jeffrey Snyder,[d] Gian-Marco Rignanese,[c] Anubhav Jain[b] and Mary Anne White[a,h,i] *

a Department of Physics and Atmospheric Science, Dalhousie University, 6310 Coburg Rd, PO BOX 15000, Halifax, NS, B3H 4R2 Canada

b Lawrence Berkeley National Lab, 1 Cyclotron Rd, Berkeley, CA, USA

c Institute of Condensed Matter and Nanosciences (IMCN), Université catholique de Louvain, Chemin des Étoiles 8, B-1348 Louvain-la-Neuve, Belgium

d Department of Materials Science and Engineering, Northwestern University, 2220 Campus Drive, Evanston, IL-60208, USA

e Department of Chemistry, Koc University, Sariyer, Istanbul 34450, Turkey

f State Key Laboratory of Advanced Technology for Materials Synthesis and Processing, Wuhan University of Technology, Wuhan 430070, China

g Department of Applied Physics and Materials Science, California Institute of Technology, 1200 E. California Blvd. Pasadena, CA 91125, USA

h Clean Technologies Research Institute, Dalhousie University, Halifax, NS B3H 4R2, Canada

i Department of Chemistry, Dalhousie University, Halifax, NS B3H 4R2, Canada

*Author for correspondence; email: mawhite@dal.ca; Tel: 902-494-3894; website: http://mawhite.chem.dal.ca/

Abstract: There still exists a crucial need for new thermoelectric materials to efficiently recover waste heat as electrical energy. Although metal phosphides are stable and can exhibit excellent electronic properties, they have traditionally been overlooked as thermoelectrics due to expectations of displaying high thermal conductivity. Based on high-throughput computational screening of the electronic properties of over 48,000 inorganic compounds, we find that several metal phosphides offer considerable promise as thermoelectric materials, with excellent potential electronic properties (e.g. due to multiple valley degeneracy). In addition to the electronic band structure, the phonon dispersion curves of various metal phosphides were computed indicating low-frequency acoustic modes that could lead to low thermal conductivity. Several metal phosphides exhibit promising thermoelectric properties. The computed electronic and thermal properties were compared to experiments to test the reliability of the calculations indicating that the

predicted thermoelectric properties are semi-quantitative. As a complete experimental study of the thermoelectric properties in MPs, cubic-NiP_2 was synthesized and the low predicted lattice thermal conductivity (~1.2 W m^{-1} K^{-1} at 700 K) was confirmed. The computed Seebeck coefficient is in agreement with experiments over a range of temperatures and the phononic dispersion curve of c-NiP_2 is consistent with the experimental heat capacity. . The predicted high thermoelectric performance in several metal phosphides and the low thermal conductivity measured in NiP_2 encourage further investigations of thermoelectric properties of metal phosphides.

1. Introduction

More than half of the energy produced worldwide is lost as waste heat and recovering even a fraction of that energy would have an enormous impact. Thermoelectrics (TEs) can harvest waste heat by converting thermal energy to electrical. While TE materials have been known for almost a century and have been applied in diverse areas such as space exploration and the automotive industry, they are not widely used due to their low efficiency and relatively high cost. Therefore, exploration for new TE materials remains important.

The TE efficiency is related to the dimensionless figure of merit,

$$zT = \frac{S^2 T}{\rho \left(\kappa_e + \kappa_p \right)}$$

(1)

where ρ is the electrical resistivity, S is the Seebeck coefficient, T is the absolute temperature, and κ_e and κ_p are the electronic and phononic contributions to the thermal conductivity, respectively.[1] The electronic properties are closely related to the carrier concentration and the electronic band structure. For enhanced TE performance, multiple valley degeneracy in the electronic band structure and an optimization of the carrier concentration are required.[2] In addition to enhanced electronic properties, κ_p has to be minimized. Although several strategies can be applied to reduce the thermal conductivity (including nanostructuring,[3] point defect scattering, and alloy scattering[4]), the thermal conductivity is limited by the amorphous limit of the material.[5,6] A reduction in κ_p due to increased scattering from such external mechanisms usually results in an increase of ρ, and thus low intrinsic thermal conductivity is preferable for TE. Some families of compounds with large unit cells and disordered structures can display low intrinsic thermal conductivities, e.g., clathrates,[7,8] Zintl pinictides,[9,10] or skutterudites,[11] but the discovery of new materials with low intrinsic κ_p and enhanced electronic properties is challenging.

A potential way to uncover new high-performance TE materials is using first-principles calculations, which have already revealed promising new materials for batteries[12], photocatalysts[13], and solar cells.[14] Computational studies of different TE families, e.g., half-[15] and full-Heusler compounds,[16] zinc antimonides,[17,18]

2

transition metal silicides,[19] and sulfides,[20] have been performed to predict the electronic properties; however, due to the complex interdependencies of TE properties, further investigations with a larger database with the inclusion of thermal properties are required. In a high-throughput screening within the Materials Project (www.materialsproject.org) we initially computed the electronic band structures and TE properties of over 9,000 compounds using a semi-classical Boltzmann transport theory with constant relaxation time.[21] In this screening, a novel class of high-performance TE materials, XYZ_2 (X,Y: rare earth or transition metals; Z: group VI element), was identified leading to an experimentally-measured zT up to 0.75.[21,22] Recently, we extended the screening of electronic properties to over 48,000 inorganic compounds.[23,24]

In the present study, we reveal a potential class of high-performance TE materials with enhanced electrical properties from this screening: metal phosphides (MPs). Although MPs are known to be stable and have excellent electronic properties [25,26,27,28] and therefore are of interest for PV/optoelectronics,[29] they are less frequently considered as potential TEs due to their expected high thermal conductivity. For instance, phosphide skutterudites (*e.g.* $CeFe_4P_{12}$) have high experimental power factors, but the TE performance is limited by the high thermal conductivity.[28] Similar behaviour was found in a theoretical study of two-dimensional black phosphorous which has an estimated high thermal conductivity leading to low zT.[30] Conversely, some MPs have low experimental thermal conductivity but with high ρ limiting zT, such as Zintl phases.[31] A lower ρ was measured for phosphide clathrates, which have also exhibited low thermal conductivities due to rattling mechanisms of the guest atoms [32,33]. In a recent study, the TE properties of $Ag_6Ge_{10}P_{12}$ were investigated indicating relatively high zT (~0.6). $Ag_6Ge_{10}P_{12}$ displays low thermal conductivity due to its complex crystal structure and enhanced electronic properties suggesting that phosphides can show promising TE performance.[34]

To search beyond these previous studies, the TE properties of several subclasses of MPs, which have not considered yet for TE materials, are investigated in this study: XP, XYP, XP_2, and X_3P_2, where X is a metal and Y is an alkali metal. For a more complete prediction of the TE performance, in addition to the electronic properties, we estimated κ_p by different methods. The theoretical lowest limit (κ_{min}) was computed using the Cahill-Pohl model[5,6] and a recent developed model to explain ultralow thermal conductivity. In this model the phonon mean speed is averaged over the entire phonon dispersion curve and the phonon mean free path is frequency-independent and limited by static disordering, *i.e.* atomic distribution in the unit cell.[35] The latter model was modified in this study using a frequency-dependent phonon mean free path limited by dynamic disordering, *i.e.* Umklapp scattering. For more crystalline samples, κ_{min} underestimates κ_p and thus, a semi-empirical approach was used as described by Miller *et al*.[36] While the semi-empirical approach shows more an average thermal conductivity of the material, κ_p approaches κ_{min} at high temperatures or small grain sizes and should be considered as a lower bound. The computed electrical and thermal properties revealed that several MPs indicate high TE performance. In particular, XYP compounds have high predicted power factors and low thermal conductivity, regardless of the thermal

conductivity model used to calculate the TE performance. As a proof of concept for the prediction of MPs, the computed electronic and thermal properties are compared to literature. The reported experimental electronic properties of various XP_2 compounds (*e.g.*, CuP_2, IrP_2 and RuP_2) and X_3P_2 (*e.g.*, Cd_3P_2 and Zn_3P_2) indicate good agreement with the computed values. In particular, IrP_2 and Cd_3P_2 have high experimental power factors at room temperature, despite their low carrier concentration. The high power factor of Cd_3P_2 is especially interesting as low thermal conductivity was measured in a separate study. Recent studies have even demonstrated that κ_p in Zn_3P_2 can be dramatically reduced by nanostructuring, even below the predicted κ_{min}, and that ρ is not affected by the crystallinity in Zn_3P_2 thin films. [37,38] Herein, we present that the low thermal conductivity in Zn_3P_2 can be delineated with the phonon dispersion curve using no fitting parameters. Most of the published studies, however, reported the electronic or thermal properties only in a small temperature range and coherent data is necessary to avoid discrepancy between samples. For a complete thermoelectric study, we synthesized the cubic-phase of NiP_2 (*c*-NiP_2) which has an experimental κ_p below κ_{min} while ρ remains low over a wide temperature range. Although *c*-NiP_2 has low predicted TE performance, due to its isotropic properties and small band gap, no doping is required and the intrinsic properties can be compared to computations indicating good agreement with the temperature-dependent Seebeck coefficient and lattice thermal conductivity.

2. Computational and Experimental Details

2.1. Electronic Band Structure and Phonon Dispersion Curve Calculations

The electronic band structures and electron localization function (ELF) were computed using the Vienna *ab initio* Simulation Package (VASP)[39] with the Perdew–Burke–Ernzerhof (PBE) generalized gradient approximation (GGA)[40] and projector augmented-wave (PAW)[41] method to model core electrons. For an improved prediction of the band gap energy, the electronic band structures also were computed with the hybrid functional HSE06.[42,43] The electronic transport properties were calculated using the PBE and HSE band structures and the BoltzTraP code[44] with a constant relaxation time of $\tau = 10^{-14}$ s and a carrier concentration of 10^{20} cm^{-3} in the temperature range between 300 K and 1300 K. These assumptions were also applied in our previous study where a strong correlation was found between predicted Seebeck coefficient and experiments.[23] All computations and data analyses were performed using the high-throughput calculation software developed in Python: pymatgen,[45] FireWorks,[46,46] and atomate [47]. Further details regarding the computations are described in references [21,23].

The elastic properties, including the 6×6 elastic tensor, shear and bulk moduli, were calculated using DFT. Perturbations were applied to the lattice vectors, allowing for relaxation of the ions, then the resulting stress tensor was calculated from DFT. Finally, linear elasticity relations were used to fit the elastic tensor using the Green-Lagrange strain tensor. More details on the elastic properties calculations and tested results are available elsewhere

(https://materialsproject.org/docs/calculations).[48] The stretching force constants were obtained using the Alloy Theoretic Automated Toolkit (ATAT) code.[49]

To calculate the Bader charges, we used the code developed by Henkelman group.[50] This method implements a grid-based algorithm method that follows the steepest ascent path in the charge density gradient between the grid points to determine an atom's Bader volume. It then calculates the charge of the atom by integrating the charge density computed via DFT. Further information can be found in reference [51].

Phonon dispersion curves and thermodynamic properties were computed using the ABINIT package[51] within the framework of density functional perturbation theory (DFPT).[52,53,54] Norm-conserving pseudopotentials were employed [55] and exchange correlation interactions were taken into account using the PBE-GGA approximation.[41] The Grüneisen parameter was calculated using the following definition:

$$\gamma = \sqrt{\frac{\sum_q \sum_i^{\hbar\omega_{iq}<k_B\theta_D} \gamma_{iq}^2 C_{iq}}{\sum_q \sum_i^{\hbar\omega_{iq}<k_B\theta_D} C_{iq}}} \qquad (2)$$

where γ_{iq} are the Grüneisen parameters for each band and q point, obtained as the finite difference derivative of the phonon frequencies. These have been calculated at different volumes. C_{iq} is the mode heat capacity and the sums are limited to the modes with an energy lower than the one corresponding to the Debye temperature, θ_D.[56,57]

2.2. Sample Preparation

The cubic phase of nickel diphosphide, c-NiP$_2$, which is stable at low temperatures and high pressures, was synthesized using high-energy ball milling. Elemental Ni (0.97 g, <150 micron, 99.99%, Sigma Aldrich) and red P (1.153 g [6 mass% more than the stoichiometric requirement], 99.7%, Sigma Aldrich) were placed in a hardened steel vial with six ½ inch hardened steel balls (~33 g) under argon atmosphere. The milling time was set to 6 hours and 15 minutes in an SPEX model 8000-D and the vials were opened in argon atmosphere. The product was a black powder, yield >90%. The powder was consolidated to a pellet using a pressure of ~1.1 GPa for 15 minutes at room temperature and under air atmosphere. For the low-temperature transport property measurements, the consolidated pellets were sealed in an evacuated glass tube and heated to 600 °C for 2 hours, followed by slowly cooling to room temperature.

2.3. Sample Characterization

The crystal structure was investigated using a Rigaku Ultima IV diffractometer, equipped with a Cu Kα (λ = 1.541 Å) X-ray source, a graphite monochromator, and a

scintillator. The lattice parameters were refined using the software package Rietica.[58] The density was determined with the Archimedes' principle. To investigate the microstructure, a Hitachi S4700 cold-field emission scanning electron microscope with an Oxford Inca energy dispersive X-ray analysis system was used. The thermal decomposition was determined with a Netzsch TG 209F3 under constant argon flow using a sample mass of ~13 mg and a scanning rate of 10 K min^{-1}. The heat capacity (2 to 300 K: 27.82±0.01 mg; 0.4 to10 K: 21.01±0.01 mg) was determined using a Quantum Design Physical Property Measurement System (PPMS) from 0.4 K to 300 K under high vacuum (10^{-7} bar). The relaxation calorimetry technique for both ^{4}He and ^{3}He cooling is described in detail elsewhere.[59]

2.4. Measurements of Transport Properties

The low-temperature transport properties were measured under steady-state conditions from 2 K to 325 K with a PPMS under high vacuum. The thermal transport option was used to measure the electrical resistivity, Seebeck coefficient, and thermal conductivity simultaneously. A consolidated pellet (diameter = 5.10 ± 0.04 mm, thickness 1.12 ± 0.04 mm, and density of 4.04 ± 0.2 g cm^{-3}) was adhered between two gold-plated copper disks with silver epoxy (Tra-Bond 2902) and fixed on the thermal transport stage. While ρ and thermal conductivity [60,61] were determined from the geometry dimensions and the electrical resistance and thermal conductance, respectively, the S was measured from the voltage drop by applying a temperature gradient. The thermal conductivity was corrected assuming an emissivity of one due to blackbody radiation.

For the transport properties from 300 K to 725 K, a different consolidated pellet (diameter = 5.10 ± 0.04 mm, thickness = 1.12 ± 0.04 mm, and density 4.04± 0.2 g cm^{-3}) of the same powder was used. The electrical resistivity and the Hall coefficient (magnetic field of 2 T) were measured with the van der Pauw technique and pressure-assisted molybdenum electrodes, as described elsewhere.[62] The high-temperature S measurements were performed using chromel-niobium thermocouples by applying an oscillated temperature gradient of ±7.5 K.[63] The thermal diffusivity, α, was determined using a Netzsch LFA 457 laser flash apparatus and the thermal conductivity was calculated from $\kappa = \alpha \bullet d \bullet C_p$, where d is the mass density and C_p is the heat capacity under constant pressure. For C_p, we used the computed heat capacity together with the electronic contribution to the heat capacity determined from experiments.

3. Results and Discussion

3.1. Electronic Band Structure and Computed Electrical Properties

From the high-throughput screening, it was observed that several metal phosphides (MPs) are predicted to have high PFs (see Table S1 and S2). Here, we present further computational investigation on 26 compounds. These compounds can be separated into different subclasses: XP, XYP, XP$_2$, and X_3P$_2$, where X is a metal and Y is an alkali metal. The PBE-GGA electronic band structures, not shown here, can be obtained in the open database of the Materials Project (http://www.materialsproject.org).[64] The computed electronic properties of 48,000 inorganic compounds including MPs have

been recently published.[24] All electronic properties here were calculated with a universal constant relaxation time of $\tau = 10^{-14}$ s and for a carrier concentration of 10^{20} cm^{-3}.

Within the XP group, both the p-type PF (p-PF) and n-type PF (n-PF) of GaP ($F\acute{4}3m$, mp-2490) and BP ($F\acute{4}3m$, mp-1479) stand out in the computational screening. The power factors (using a constant relaxation time) are relatively high within the class of isotropic band structures due to the parabolic band curves. The strongly curved valence bands in BP and GaP, as also discussed by Varley $et\ al.$,[65] are multi-valley degenerate at Γ, resulting in a high p-PF (Figure 1 (a)). GaP exhibits multiple band degeneracy in the conduction bands with a valley degeneracy of 4 at L (conduction band minimum) and a second minimum along Γ-X at 0.054 eV above the conduction band minimum with a multiplicity of 6 (Figure 1 (b)). Together with the low predicted ρ (0.96 mΩ•cm for GaP and 1.3 mΩ•cm for BP, respectively, at 600 K and assuming a carrier concentration of $n = 10^{20}$ cm^{-3} and relaxation time of $\tau = 10^{-14}$ s) the predicted n-PFs in GaP and BP are relatively high (6.45 and 4.19 mW m^{-1} K^{-2}, respectively). InP, on the other hand, exhibits only high p-PF due to multi-degeneracy at the Γ-point. The n-PF is limited due to a low Seebeck coefficient resulting from a single-degenerate band at the Brillouin zone center whereas ρ is as low as GaP and BP. Low ρ is typical for most III-V semiconductors where the Fermi surface is often spherical resulting in uniformly low effective mass.[66] However, a high electrical conductivity also leads to a high electronic contribution of the thermal conductivity at high temperature ($\kappa_e > 1$ W m^{-1} K^{-1}) which could limit the performance as TE materials.
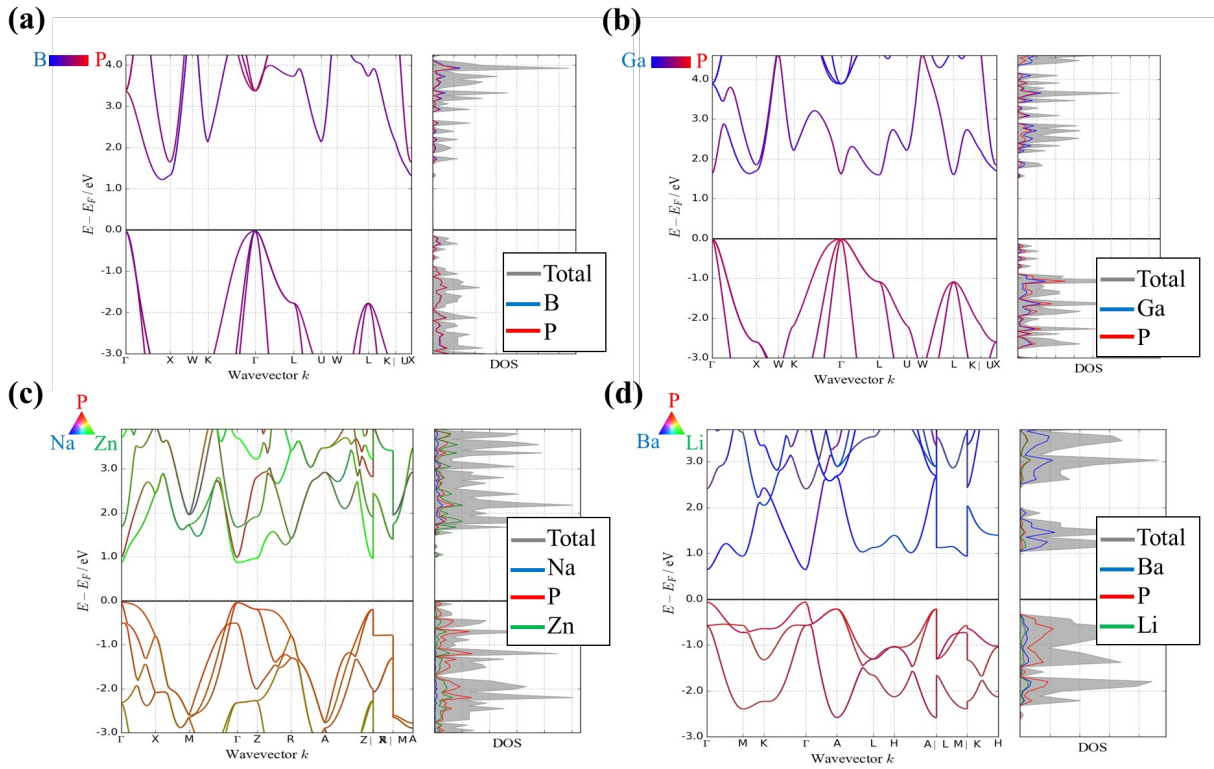
Figure 1: Calculated electronic band structure of (a) BP ($F\acute{4}3m$, mp-1479), (b)

GaP ($F\overline{4}3m$, mp-2490), (c) ZnNaP ($P4/mmm$, mp-4842), and (d) BaLiP ($P\overline{6}m2$, mp-10615) computed with DFT-PBE.

One of the most interesting characteristics of XYP compounds, including SrLiP ($P\overline{6}m2$,mp-10614), BaLiP ($P\overline{6}m2$,mp-10615), and SnNaP ($P6_3mc$,mp-29529), is their highly anisotropic conduction, especially at valence band maxima (see Figure 1 (c) and (d); Table S3) resulting in relatively high predicted p-PF. Anisotropy in the present MPs leads to high PF due to distorted electron/hole pockets.[67] Although the density of states effective mass varies by less than a factor of two in different directions, leading to a small anisotropic Seebeck coefficient , the band effective mass varies by more than an order of magnitude in different directions, *i.e.* increasing the electrical conduction and improving PF in certain direction(s). Furthermore, we calculate that for XYP compounds at higher temperatures multiple valleys in the electronic band structure may contribute to the carrier transport, making S as extreme as -400(-370) and 394(365) μV K^{-1} in LiBaP(ZnNaP), respectively, at a carrier concentration of 10^{20} cm^{-3} and a temperature of 1300 K while the curvature of the bands results in a low effective mass and low ρ.

The XP$_2$ compounds reveal high calculated PFs for both phases of NiP$_2$, the cubic phase ($Pa\overline{3}$,c-NiP$_2$, mp-22619) and the monoclinic phase ($C2/c$, m-NiP$_2$, mp-486) as indicated by Fermi surface in Figure 2 (a) and (b), and the electronic band structures in Figure S1 in Supplementary Information. Whereas c-NiP$_2$ has several pockets in the conduction band, the conduction band in m-NiP$_2$ exhibits several pockets near the Brillouin zone center at elevated temperature (>600 K) enhancing the TE performance. Furthermore, the valence bands in m-NiP$_2$ have eight pockets at the Brillouin zone edge. Calculations estimate that these phases will generally exhibit a low ρ at low temperature except n-type for the monoclinic phase. In terms of the Seebeck coefficient, we expect that the zero band gap calculated in PBE-GGA results in an enhanced bipolar effect: although c-NiP$_2$ has several pockets (Figure 2 (a)) the predicted magnitude of the Seebeck coefficient is relatively small (~50-80 μV K^{-1}) between 400 K and 1300 K. Conversely, m-NiP$_2$ has a relatively high calculated Seebeck coefficient (~360 μV K^{-1}) at low temperature (500 K) and high carrier concentration (10^{20} cm^{-3}) demonstrating that it is a potential candidate for low-temperature thermoelectrics. Other XP$_2$ monoclinic materials, including BeP$_2$ ($C2/c$, mp-27148) and PdP$_2$ ($C2/c$, mp-28266), also possess a multi-valley band structure. However, the PdP$_2$ band structure is much more anisotropic than that of BeP$_2$ and predicts a larger n-PF and p-PF in certain directions than BeP$_2$. PdP$_2$ crystallizes in a layered structure resulting in an anisotropic band structure similar to NiP$_2$ whereas BeP$_2$ has a more symmetric bulk crystal structure.

It should be noted that the conduction bands of CoP$_2$ ($P2_1/c$, mp-14285) and AgP$_2$ ($P2_1/c$, mp-8200) as well as the valence bands of CuP$_2$ ($P2_1/c$, mp-927), IrP$_2$ ($P2_1/c$, mp-10155) and RhP$_2$ ($P2_1/c$, mp-1413) are calculated to be multi-valley degenerate, leading to higher n- and p-PF, respectively. The Fermi surfaces at the conduction bands of AgP$_2$ and IrP$_2$ are flat in one dimension and dispersive in the other two directions (Figure 2 (c) and (d)). Whereas the two hole pockets of AgP$_2$ are

dispersive near the center of the Brillouin zone increasing the electronic performance (PF = 3.40 mW m^{-1} K^{-2} at 1100 K and 10^{20} cm^{-3}), the four hole pockets of IrP$_2$ are dispersive in-plane enhancing the electronic performance due to a higher degeneracy (PF = 5.23 mW m^{-1} K^{-2} at 1100 K and 10^{20} cm^{-3}). Furthermore, both valence and conduction bands in ZnP$_2$ ($P4_12_12$, mp-2782; $P4_32_12$, mp-11025) and the valence in FeP$_2$ (*Pnnm*, mp-20027) are multi-valley degenerate. Unfortunately, the flatness of the bands increases the band effective mass in the conduction band limiting the thermoelectric performance due to relatively high computed ρ (>5 mΩ cm at low temperatures).

Most of the X_3P$_2$ compounds have a direct band gap and a high degeneracy in the valence bands at the Γ-point. In particular, Zn$_3$P$_2$ ($P4_2/nmc$, mp-2071) exhibits curved bands with some slightly lower-energetic valleys leading to high calculated *p-PF* at ambient temperatures (4.4 mW m^{-1} K^{-2} at 900 K and 10^{20} cm^{-3}). The conduction bands, on the other hand, however, are generally parabolic resulting in low ρ while at high temperature multi-valleys contribute to the electrical properties and hence high calculated *n-PF*, *e.g.* 5.4 mW m^{-1} K^{-2} for Mg$_3$P$_2$ ($Pn\bar{3}m$, mp-8085) at 1300 K and 10^{20} cm^{-3}.
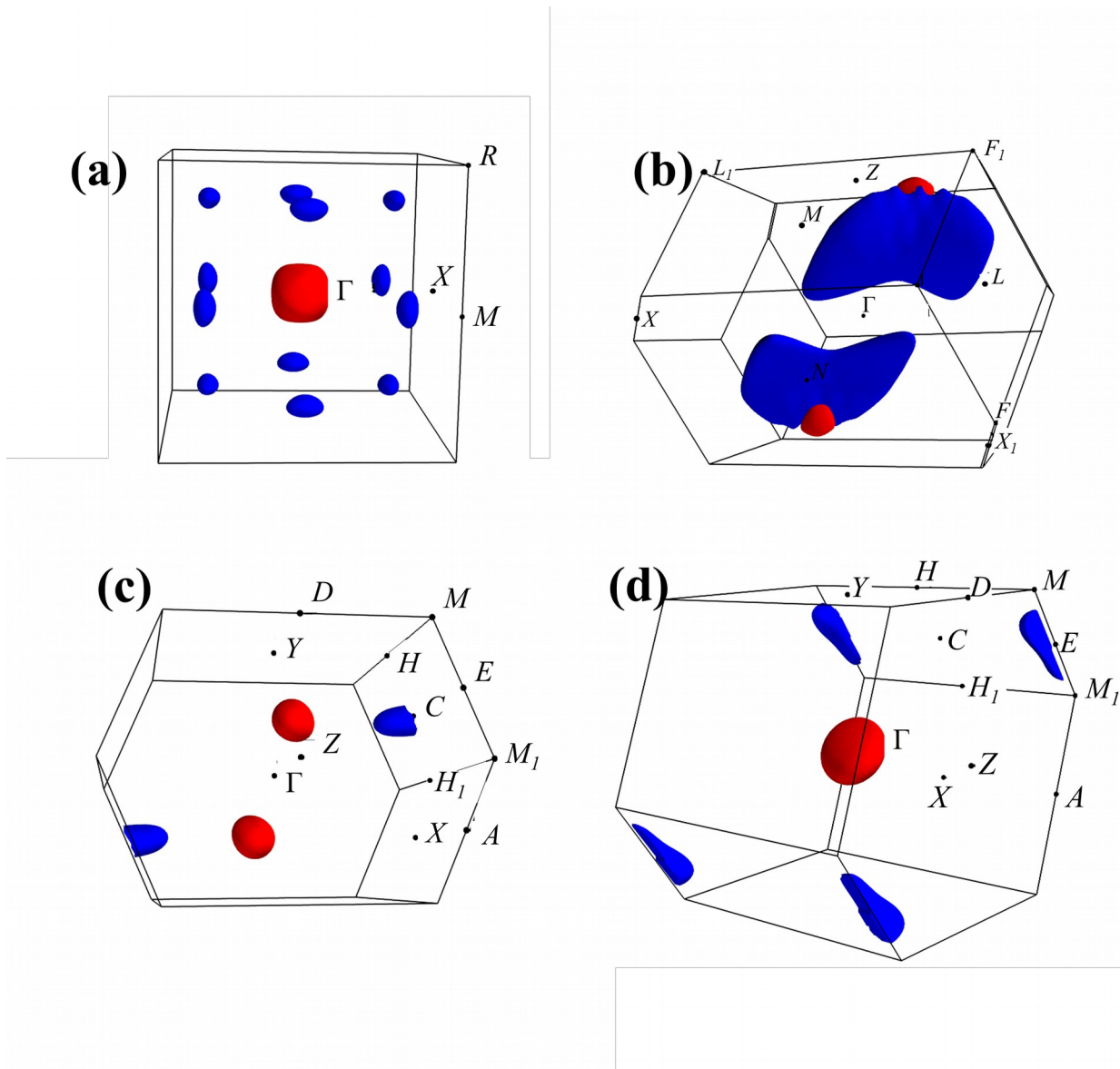
Figure 2: Fermi surfaces of (a) c-NiP$_2$ ($Pa\bar{3}$, mp-22619 (b) m-NiP$_2$ ($C2/c$, mp-486), (c) AgP$_2$ ($P2_1/c$, mp-8200), and (d) IrP$_2$ ($P2_1/c$, mp-10155) computed with PBE-GGA using a cut-off energy of 0.05 eV. Multiple pockets at the VBM (blue) are mostly at the Brillouin zone edge while the pockets of the CBM (red) are at the Γ point.

We note that band structures were calculated with the PBE-GGA exchange functional which typically underestimates the experimental band gap energies.[67,68] Some of the band structures (see Tables S1 and S2) were also calculated using the more accurate HSE06 exchange functional, and an increase in the band gap energies was observed. The average increase in band gap energy of semiconducting MPs using the HSE functional as compared to PBE-GGA was 0.76 eV. This is consistent with the study by Chan and Ceder which reported that the PBE-GGA

10

exchange functional underestimated the band gap energy on average by 0.73 eV compared to experimental determined band gap energies.[69] The HSE06 exchange functional typically overestimates slightly the band gap energies compared to experiments and a smaller discrepancy between the present study and the study by Chan and Ceder is expected. Furthermore, Setyawan *et al.* found a relative uncertainty of 42% in large band gap energy systems, which is consistent with the relative error of MPs (48%), although the band gap energies are in the range of 0.3 – 1.6 eV (1.1-2.2 eV with HSE).[70] For most compounds investigated here, the underestimation of the band gap energy makes only a slight change in the predicted thermoelectric performance at 600 K. While the *p-PF* and *n-PF* increases for ZnP_2 (mp-2782, mp-11025) at 600 K with the inclusion of HSE a reduction of the *PF*s in AgP_2 (mp-8200) was predicted for *p*-and *n*-type, as shown in Table S4. In other materials, an increase in the *PF* was observed for *p*-or *n*-type, whereas the *PF* of the opposite type decreases.

3.2. Phonon Dispersion Curve and Computed Thermal Conductivity

In addition to the electronic band structures, the phonon dispersion curves of 10 MPs were computed to provide basic information about the thermal conductivity. The phonon dispersion curves indicate that more complex unit cells have low-frequency acoustic phonons that are suppressed by optical modes and avoided band crossing, as illustrated for AgP_2 and Zn_3P_2 in Figure 3 (a) and (b), leading to a reduction in the phonon mean speed. The phonon dispersion curves of BP and GaP (Figure 3 (c) and (d)) are similar to that of diamond structure (Si, Ge)[71] and III-V semiconductors, *e.g.*, GaAs,[72] where a large split of the longitudinal and transverse acoustical phonons appears. Although the transverse modes have zero group velocity at the Brillouin zone edge, all three acoustic phonons have similar speed of sound at the Brillouin zone center, increasing the thermal conductivity for materials with long phonon mean free paths. High thermal conductivity of the *X*P compounds is also expected from the split of the acoustic and optical phonons. Because of the large phonon band gap, the acoustic phonons are less coupled to the optical phonons and therefore the scattering of the acoustic phonons is reduced, increasing the phonon mean free path.[73,74,75] It is important to note that all optical modes are nearly flat in the calculated MP phonon dispersion curves, *i.e.*, the optical modes do not contribute substantially to the thermal conductivity.

Although phonon dispersion curves can be computed with high-throughput approaches, the added computational costs for the calculation of third-order force constants currently limits first-principles determination of the thermal conductivities (with exceptions for simple crystal structures).[76,77,78] Therefore, the thermal conductivity was estimated with approximate and semi-empirical models enhancing the prediction of novel high-performance thermoelectric materials.[5,6,37,37] For example, the thermal conductivity has been tested with models for the amorphous limit of the thermal conductivity. The most established model to determine the amorphous limit is the Cahill-Pohl model [5,6] where the speed of sound was calculated from the bulk and shear moduli of the materials (see Supplementary Information). In addition to the elastic properties, the minimum thermal conductivity was also calculated using the linear slope of the acoustic phonons at the Brillouin center and the Cahill-Pohl model where the speed of sound was averaged from the

longitudinal and transverse phonons (see Supplementary Information Equation SI-4). In an earlier study, it was found that the computed κ_{min} has a strong correlation with the experimental κ_p.[23] However, several materials exhibited lower thermal conductivity than the predicted amorphous limit; the thermal conductivity in these materials is defined as 'ultralow'.[79] In a recent study, the origins of the ultralow thermal conductivity of [6,6]-phenyl-C_{61}-butyric acid methyl ester (PCBM) were delineated.[36] The thermal conductivity in this model is limited by an average phonon mean speed over the entire Brillouin zone and the atomic density. While a constant phonon mean free path can represent the limit for disordered structure, *i.e.* static disordering (referred as 'static'), a frequency-dependent mean free path can most likely describe the thermal conductivity where dynamical disordering is the limiting factor (referred as 'dynamic'). (Details about the models are given in the Supplementary Information). The static and dynamic model exhibit lower κ_{min} than the Cahill-Pohl model (Table S5). In particular, κ_{min} in *X*P compounds is significantly decreased due to the reduced phonon mean speed at the Brillouin zone edge, as shown in Figure 3 (c) and (d).
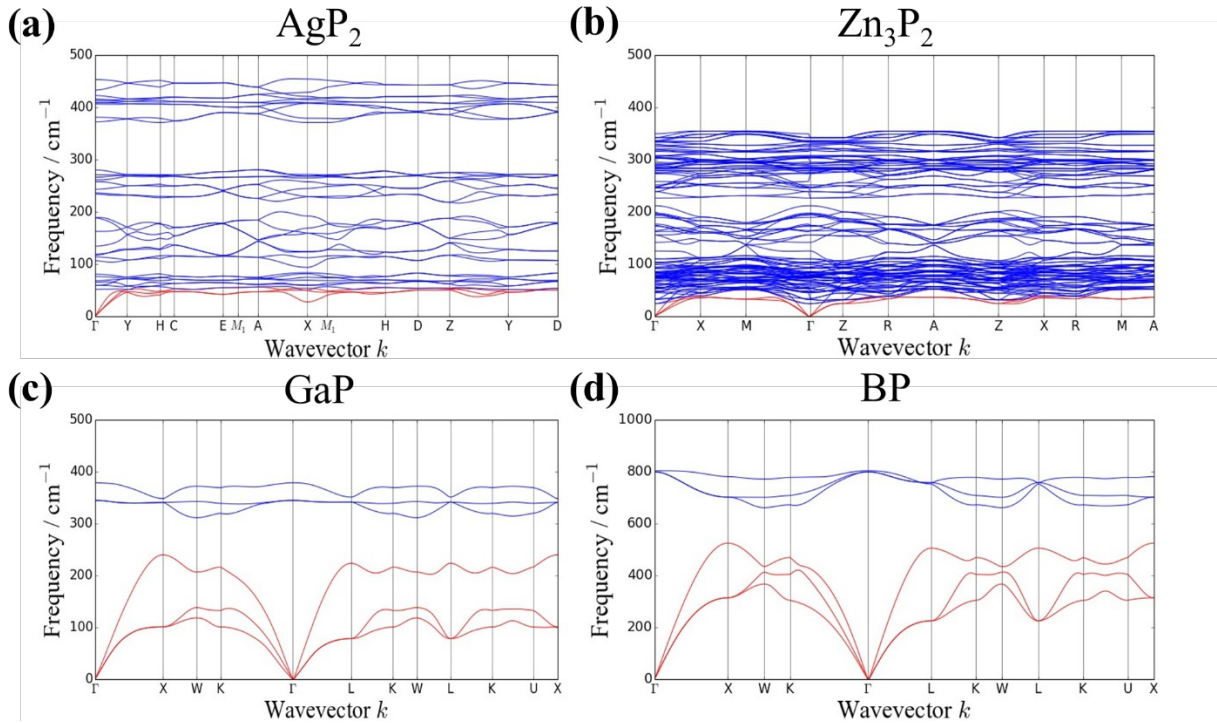

Figure 3: Calculated PBE-phonon dispersion curve of (a) AgP_2, (b) Zn_3P_2, (c) GaP, and (d) BP. Note that the scale of the *y*-axis in (d) is twice that of the other band structures. Although GaP possesses a simple crystal structure, the calculated minimum thermal conductivity using the average phonon mean speed is low due

to splitting of the longitudinal and transverse acoustic modes.

In addition to the amorphous limit, the thermal conductivity of the MPs was computed with a semi-empirical model as recently reported by Miller *et al.*[37] In this approach, the thermal conductivity equation contains information of the lattice stiffness and crystal structure computed with DFT and was fitted to experimental data at 300 K. The Grüneisen parameter used for the prediction of the thermal conductivity is solely dependent on the coordination number.[37] A similar trend was observed by Zeier *et al.* [80] While the amorphous limit describes the lower bound of the thermal conductivity, the semi-empirical approach provides an average thermal conductivity more suited for crystals limited by acoustic phonons. For a better comparison of the MPs, the semi-empirical approach at 300 K was compared to the amorphous limit using the Cahill-Pohl model (computed thermal conductivity data in Table S6).

As shown in Figure 4, the thermal conductivity from the semi-empirical model (κ_{SE}) is exponentially related to the amorphous limit for most of the MPs, *i.e.,* low κ_{min} would also result in a low κ_{SE} for most compounds. However, based on the semi-empirical model some MPs have a higher thermal conductivity (such as GaP and BP (κ_{SE} = 48 and 244 W m^{-1} K^{-1}, respectively)), or similar thermal conductivity (BeP$_2$) compared to the amorphous limit. It is important to note that for κ_p in MPs only the acoustic phonons were considered. The semi-empirical approach has two terms, a temperature-dependent term and temperature–independent term which represents the amorphous limit. While *X*P compounds have relatively high thermal conductivities at 300 K, *e.g.*, κ_{SE} = 47.74 W m^{-1} K^{-1} for GaP, a lower thermal conductivity was predicted for *X*P$_2$ (~5-15 W m^{-1} K^{-1}), *X*$_3$P$_2$ (2-4 W m^{-1} K^{-1}) and *XY*P compounds (~2 W m^{-1} K^{-1}) at 300 K. In particular, the low thermal conductivities of *XY*P compounds are in the range of PbTe suggesting promising TE performance.
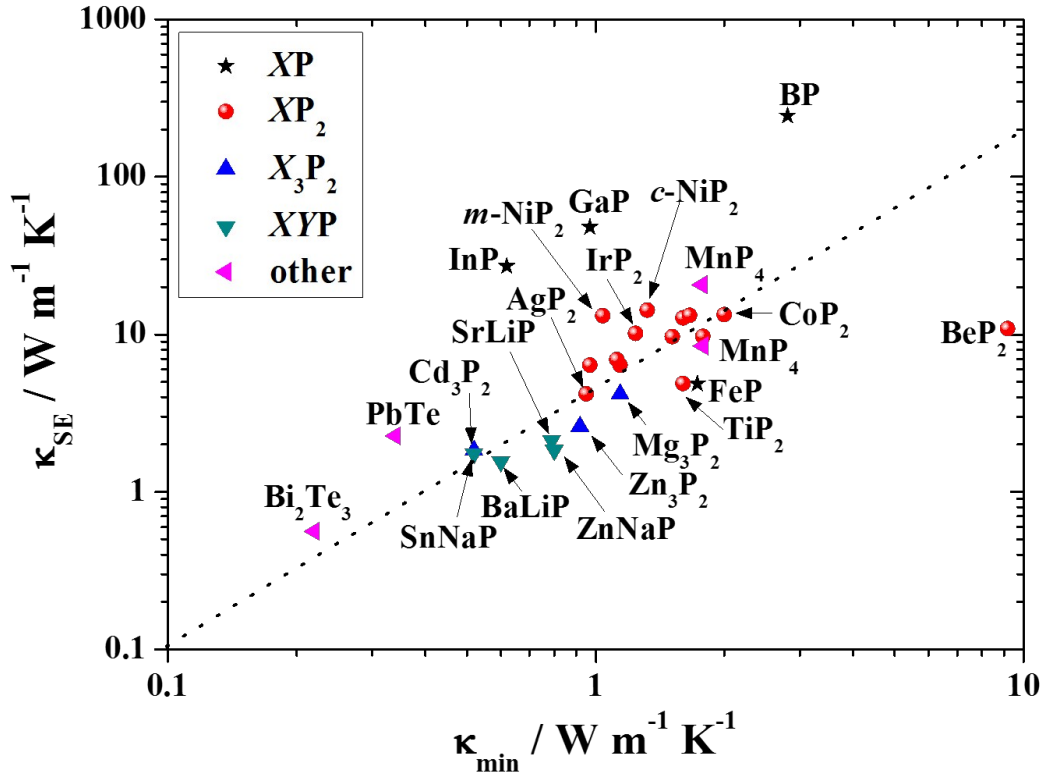
Figure 4: Thermal conductivity computed using the Cahill-Pohl model (κ_{min}) [5,6] and a semi-empirical approach (κ_{SE}) at 300 K of various MP classes.[37] Computed thermal conductivities are given in Table S6.

3.3. Thermoelectric Performance

The electronic and phonon properties of the MPs were summarized in a theoretical figure of merit ($zT_{calc} = \dfrac{S^2 T}{\rho\left(\kappa_p + \kappa_e\right)}$) and compared to the current-best TE materials (Bi_2Te_3 and PbTe). For the prediction of κ_p we use κ_{min} and κ_{SE} as the optimum and the average case. zT_{calc} is different from the TE figure of merit, zT. Although the defining equation of zT_{calc} is nearly the same as for zT (if κ_p is set to κ_{min} or κ_{SE}), several assumptions were employed to quantify the transport properties. For instance, the electronic properties were computed with the Boltzmann transport equations with the relaxation time was set to $\tau = 10^{-14}$ s. This value is typical for metals at room temperature and has the advantage of providing a power factor, *PF*, for comparison with experiment. In the constant relaxation time approach, the Seebeck coefficient is treated as independent of the relaxation time, while both the electrical conductivity and the electronic contribution to the thermal conductivity scale linearly with the relaxation time. However, it is important to note that the relaxation time can differ between materials/samples as it depends on diverse scattering mechanisms such as grain boundaries, electron-phonon interactions, and impurities. In particular, electron-phonon scattering can have a large influence on

14

the relaxation time. Furthermore, the relaxation time is neither independent of temperature nor energy. Thus, the reported predicted PFs and zT_{calc}s using a constant relaxation time should be treated with due caution. This is consistent with our recent study in which a significant overestimation of the computed mobility was observed compared to the literature.[23]

Both zT_{calc}s (with κ_{min} [$zT_{calc}(\kappa_{min})$] and κ_{SE} [$zT_{calc}(\kappa_{SE})$]) indicate higher predicted n-type thermoelectric performance for various XYP than the computed zT_{calc} of state-of-the-art TE materials, $i.e.$, PbTe and Bi_2Te_3 (Figure 5). As discussed above, XYP compounds have high Seebeck coefficient at elevated temperatures due to multiple band degeneracy with the assumption of a carrier concentration of 10^{20} cm^{-3} and a low predicted κ_{min}/κ_{SE}. The thermal conductivity is only slightly reduced using the semi-empirical approach compared to the lowest limit of the thermal conductivity. In particular, BaLiP exhibits high theoretical p- and n-type thermoelectric performance with a predicted zT_{calc} similar to that of PbTe and higher than that of Bi_2Te_3 for both types. For the electronic properties of the XYP compounds, the average of the electrical conductivity was considered for the calculation of PF. Due to the high anisotropic behavior of XYP compounds (Table S3), the predicted zT_{calc} can dramatically increase in certain crystallographic directions and an experimental study of single crystalline XYP is desirable.

Enhanced electronic properties were also observed in XP (except FeP due to its zero band gap) , if n can be $\geq 10^{20}$ cm^{-3}. However, although the choice of thermal conductivity model has only minor influence on the qualitative ranking of predicted zT_{calc} of XYP compounds, the thermoelectric performance of GaP and BP decreased by a factor of five and 10, respectively, from $zT_{calc}(\kappa_{min})$ to $zT_{calc}(\kappa_{SE})$ (Figure 5). n-type $zT_{calc}(\kappa_{min})$ of GaP is in the range of the best XYP compounds and nearly twice that of PbTe and Bi_2Te_3. However, with the inclusion of κ_{SE} the TE performance decreased below PbTe and Bi_2Te_3. $zT_{calc}(\kappa_{SE})$ should be considered as a better approximation of the TE performance because the scattering mechanisms of phonons and electrons are related. Assuming the lowest limit of thermal conductivity would decrease the electron relaxation time and hence, the electrical conductivity. The predicted PFs in BP is similar high for both p- and n-type, however, the high predicted lattice thermal conductivity which is consistent with the phonon dispersion curve limits the TE performance.

Enhanced TE performance was also found for several XP$_2$ ($e.g.$, AgP$_2$, CuP$_2$, PdP$_2$, and IrP$_2$) and X_3P$_2$ ($e.g.$, Mg$_3$P$_2$ and Zn$_3$P$_2$) compounds. For instance, Mg$_3$P$_2$ has parabolic conduction bands which are multi-valley degenerate, enhancing S and reducing ρ, whereas AgP$_2$ has several pockets at the conduction edge. Both MPs have relatively low thermal conductivity ($\kappa_{SE} \sim 3$ W m^{-1} K^{-1} above 1000 K). It is important to note that the electronic properties were calculated from the PBE-GGA functional and a decrease in the electronic properties was determined for AgP$_2$ using the HSE functional.
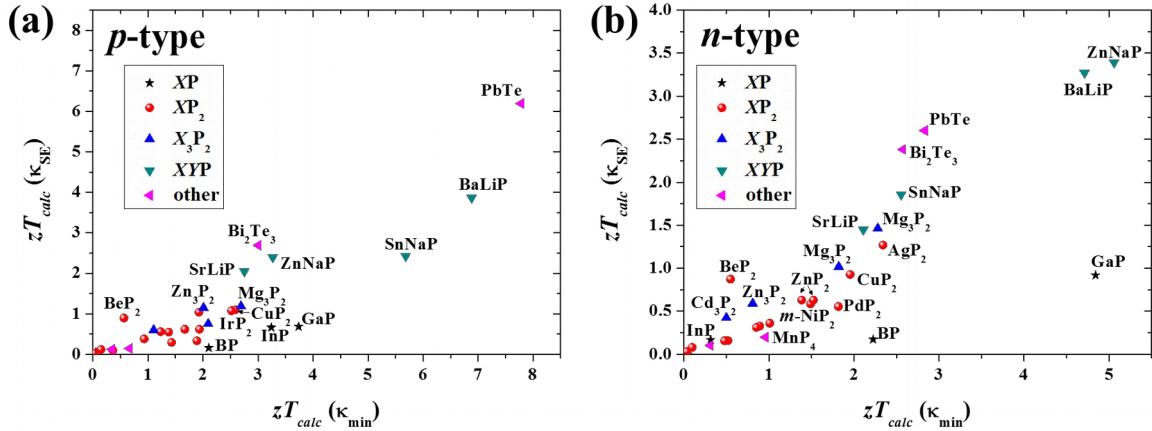
Figure 5: Comparison of computed *zT* of (a) *p*-type and (b) *n*-type MPs sorted by sub-classes. Thermoelectric figures of merit with electronic properties computed using the constant relaxation time ($\tau = 10^{-14}$ s) and thermal conductivity was estimated by the minimum thermal conductivity by Cahill and Pohl (κ_{min}) and the semi-empirical approach by Miller *et al.* (κ_{SE}) at the temperature where the predicted *zT*$_{calc}$ is maximum. Computed data are given in Tables S7 and S8.

3.4. Comparison to Literature

Our study indicates that MPs exhibit enhanced predicted electrical properties and low lattice thermal conductivity, but several assumptions (*e.g.,* relaxation time of 10^{-14} s, temperatures up to 1300 K, dopable *p-* and *n*-type up to a carrier concentration of 10^{20} cm^{-3}, minimum thermal conductivity, etc.) were used for the calculations. To determine the reliability of our assumptions, we compared the predicted electronic properties to experimental resistivities and Seebeck coefficients of various MPs using the reported carrier concentration and temperature; experimental and computed electrical properties are given in Table 1.

XP compounds indicate high predicted *PF*s due to the curved bands and multi-degeneracy at the Γ–point. However, common XP compounds such as BP, GaP, and InP can exhibit very high thermal conductivities, making them poor candidates for thermoelectric materials. For example, at room temperature, the thermal conductivities of BP, GaP, and InP are approximately 150 W m^{-1} K^{-1},[81] 77 W m^{-1} K^{-1},[82] and 70 W m^{-1} K^{-1}.[83] Our computations using a semi-empirical lattice thermal conductivity are qualitatively in-line with these observations: our calculations yield a total thermal conductivity of 245 W m^{-1} K^{-1} (243.5 W m^{-1} K^{-1} for the lattice portion) for BP, 49 W m^{-1} K^{-1} (47.8 W m^{-1} K^{-1} for the lattice portion) for GaP and 28 W m^{-1} K^{-1} (27.1 W m^{-1} K^{-1} for the lattice portion) for InP at room temperature, using a carrier concentration of 10^{20} cm^{-3} for κ_e. Furthermore, our calculations correctly reproduce that PbTe and Bi$_2$Te$_3$ possess much lower thermal conductivities: 4.2 W m^{-1} K^{-1} (2.3 W m^{-1} K^{-1} for lattice contribution) and 2.6 W

16

m^{-1} K^{-1} (0.6 W m^{-1} K^{-1} for the lattice contribution) for PbTe and Bi$_2$Te$_3$, respectively, highlighting the usefulness of these calculations for qualitative screening purposes. On the other hand, a dramatic decrease in thermal conductivity in XP compounds is predicted using κ_{min}. This is also consistent with the low thermal conductivity of XP compounds reported in literature. For instance, Kumashiro *et al.* reported a thermal conductivity of 7.5 W m^{-1} K^{-1} for BP at room temperature.[84] An even lower thermal conductivity of BP, as low as 0.4 W m^{-1} K^{-1} at 1000 K, was reported by Yugo *et al.*[85] The reported experimental thermal conductivity is only half the lowest predicted thermal conductivity (Table S5). The low thermal conductivity in BP leads to the highest experimental thermoelectric figure of merit reported for MPs (zT = 0.8 at 1000 K).[86] The experimental electrical properties of BP are in the range of the computed values (Table 1). The computed electrical resistivity and Seebeck coefficient are also compared to experiments as a function of temperature as displayed in Figure S2. The calculated resistivity is overestimated at room temperature and approaches the experimental value at elevated temperature, whereas the computed Seebeck coefficient is up to 35% higher than experiments. However, due to the large band gap BP was doped which can have a significant effect on the experimental TE properties.[85,86]

Table 1: Comparison of computed and experimental electrical properties at 300 K. Electrical properties were calculated using the Boltzmann transport equation, the PBE-GGA and HSE electronic band structures, a fixed relaxation time of 10^{-14} s and the same carrier concentration as in experiments.

Compounds	Carrier Concentration / cm^{-3}	Resistivity / mOhm cm	Resistivity / mOhm cm	Seebeck / μV K^{-1}	Seebeck / μV K^{-1}	Ref.
	Exp.	Exp.	HSE (GGA)	Exp.	HSE (GGA)	
BP	5.0•10^{18}	91	43 (43)	-300	-413 (-395)	86
BP	3.8•10^{17}	138	303 (308)	-468	-636 (-617)	85
m-NiP$_2$	8.7•10^{17}	390	99 (88)	-392	-432 (-419)	91
ZnP$_2$	1.2•10^{13}	3•10^{10}	2•10^8 (9•10^8)	n/a	1723 (1593)	86
CuP$_2$	4.3•10^{17}	126	(433)	692	(652)	91
RuP$_2$	7.4•10^{17}	90-260	(367)	-170	(-568)	90
IrP$_2$	6.9•10^{18}	7-10	(21)	250	(322)	90
Zn$_3$P$_2$	1.6•10^{17}	2200	1243 (902)	1000	724 (603)	88

Cd_3P_2	$1.3 \cdot 10^{17}$	120	305 (13)	-300	-408 (-38)	88
Cd_3P_2	$5.8 \cdot 10^{17}$	9-25	57 (12)	-200	-259 (-45)	89
c-NiP_2	$1.7 \cdot 10^{21}$	9	0.17 (0.15)	-38	-29 (-31)	Present

The very high thermal conductivities of common binary phosphides such as GaP may form the exception rather than the rule of MPs. The thermal conductivities of the binary and ternary phosphides investigated in this work are in general calculated to be 5-10 times lower than that of GaP. As one example, the total thermal conductivities of Cd_3P_2 and Zn_3P_2 (isostructural, space group $P4_2/nmc$) in our study are 7.6 W m^{-1} K^{-1} (1.8 W m^{-1} K^{-1} for the lattice portion) and 3.6 W m^{-1} K^{-1} (2.6 W m^{-1} K^{-1} for the lattice portion), respectively, and both are computed to have overall favourable TE properties. The band structures of both Zn_3P_2 and Cd_3P_2 indicate a convergence of 3 valence bands at the Γ-point as well as a secondary peak between the A and Z points that likely contribute to the favourable TE performance. For these compounds, previous experimental measurements confirm the possibilities of these compounds. Both Cd_3P_2 and Zn_3P_2 have been shown experimentally to possess moderately low thermal conductivities of 2.4 W m^{-1} K^{-1}.[87] The same study has further shown that a solid solution of these phases can reduce the thermal conductivity to as low as 1.2 W m^{-1} K^{-1}.[88] An extremely low thermal conductivity was recently reported for Zn_3P_2 (0.49 W m^{-1} K^{-1}) due to nanostructuring.[88] We tested the ultralow thermal conductivity using the various models for κ_{min}. The longitudinal and transverse speeds of sound for the Cahill-Pohl model were determined from the bulk and shear modulus (v_L = 5406 m s^{-1}, v_T = 3155 m s^{-1}). Lower phonon mean speeds for the acoustic phonons (v_L = 2755 m s^{-1}, v_{T1} = 1951 m s^{-1}, and v_{T2} = 2097 m s^{-1}) were calculated from the Zn_3P_2 phonon dispersion curve (see Figure 3 (b)), resulting in lower predicted minimum thermal conductivities (see Supplementary Information Equations SI-4 to SI-7). The experimental thermal conductivity of Zn_3P_2 (κ = 0.49 W m^{-1} K^{-1}) is lower than the amorphous limit described by Cahill-Pohl (Figure S3).[89] However, the minimum thermal conductivity using a frequency-dependent phonon mean free path agrees well with the experimental data, although the reason for the low thermal conductivity is most likely the small grain size. As stated earlier, the static disorder approach assumes that the phonon mean free path is limited by the atomic density which is smaller than the grain size. The grain size in Zn_3P_2 can be most likely further reduced leading to an even lower thermal conductivity, similar to the limit of static disordering. Therefore, it is not clear if the low thermal conductivity is due to dynamic or static disordering.

However, although Zn_3P_2 has extremely low thermal conductivity and is particularly interesting in the computational study; prior experiments indicate that a major challenge will likely be in achieving high enough carrier concentration to overcome a fairly high intrinsic resistivity (2200 mΩ•cm).[88] A better route may be to start with Cd_3P_2 due to its small band gap: a previous report has shown experimentally that at 650 K, the resistivity should be less than 5 mΩ•cm and the Seebeck coefficient should be approximate 250 µV K^{-1}, *i.e., PF* = 1.25 mW m^{-1} K^{-2} at 650 K.[89] If one conservatively assumes the measured room temperature thermal conductivity of 2.4 W m^{-1} K^{-1} [88](which would likely be reduced further at 650 K), the expected *zT* is already above 0.3. While the computed Zn_3P_2 also indicated a low TE performance due to the low carrier concentration, the enhanced TE properties of Cd_3P_2 were also predicted in our calculations. As the example of Cd_3P_2 depicts, the electronic band structures of small-band gap thermoelectrics have to be calculated with the HSE functional. While the Seebeck coefficient of Cd_3P_2 using the PBE-GGA electronic band structure are significantly are underestimated, the computed Seebeck coefficient using the HSE band structure are slightly overestimated (which is consistent with the slight overestimation of the band gap energy using the HSE functional). Thus, the Cd_3P_2-Zn_3P_2 system could be promising for future investigations.

Amongst binary compounds, IrP_2 has the second-highest *p-PF* in our study and also has its electrical properties previously characterized by experiment.[90] The band structure of IrP_2 indicates that the valence band maximum occurs with two bands at the E points (degeneracy = 1) with potentially other peaks contributing at the Z (degeneracy = 1) and C points (degeneracy = 1). Thus, this material possesses moderate valley degeneracy. A previous experimental report has determined $6.9•10^{18}$ cm^{-3} carriers at room temperature with a Seebeck coefficient of 250 µV K^{-1} and a resistivity as low as 7 mΩ•cm – *i.e., PF* = 0.89 mW m^{-1} K^{-2} at room temperature.[90] A high *PF* was also predicted in our computational study (*PF* = 0.49 mW m^{-1} K^{-2}). It is plausible that more dedicated studies of doping as well as higher temperature measurements could yield competitive *PF*s. Unfortunately, IrP_2 not only contains the extremely rare element Ir but is also computed in our study to have a moderately high thermal conductivity of 14.2 W m^{-1} K^{-1} using the semi-empirical model, making it an impractical as a TE material for widespread use. However, κ_{SE} decreases with temperature, approaching the sum of κ_{min} (= 1.24 W m^{-1} K^{-1}) and κ_e.

A more reasonable solution would be established by replacing Ir with Cu. The electrical properties of CuP_2 have been previously measured and despite the high reported electrical resistivity (ρ = 126 mΩ•cm at 300 K) due to a low carrier concentration, the experimental *p-PF* is in the range of a good TE material due to a large Seebeck coefficient.[91] The reported electrical

properties even exceed the computed values (Table 1). In addition to the favourable predicted electrical properties, the thermal conductivity of CuP_2 is reduced by a factor of two compared to IrP_2, enhancing the TE performance (Table S6). These results should encourage TE groups to investigate the TE properties further by optimizing the carrier concentration.

The ternary systems NaZnP, SrLiP, BaLiP, and NaSnP are highly interesting as either *p*-type or *n*-type thermoelectrics from a computational standpoint. Currently, these materials remain largely unexplored, although NaZnP was previously identified as a potential thermoelectric target based on calculations similar to those performed in this work.[92] Similarly, *n*-type Mg_3P_2 in the $Pn\bar{3}m$ structure could be interesting due to a convergence of multiple conduction bands at the Γ point.

We note that our screening for new phosphide thermoelectrics represents a "best-case" scenario in that we freely allow for both *n* and *p* carrier types, for the carrier concentration to reach as high as 10^{20} cm^{-3}, and assume high temperature stability up to 1300 K. Certainly, these conditions are not achievable for most phosphides. However, some materials such as InP come close: InP can be both *p* and *n*-doped beyond 10^{20} cm^{-3} and has a melting point of 1335 K.[93] The spirit of our study is to identify whether potentially promising systems exist assuming that other factors line up very well (which they very well might not). Thus, the screening is better used as tool for filtering poor thermoelectric candidates (even under optimistic conditions) rather than unambiguously identifying good candidates.

Overall, we find many possibilities within the phosphide systems, including interesting band structure characteristics (*e.g.,* high valley degeneracy in several systems) as well as potentially low thermal conductivities. Further exploration through chemical substitution and alloying could potentially uncover even more promising phosphides. It should be further noted that a recent study of $Ag_6Ge_{10}P_{12}$ (thermal conductivity is approximately 1.5 W m^{-1} K^{-1} at room temperature) has provided another experimental data point confirming low thermal conductivity and a *zT* as high as 0.6 within a phosphide system.[35] Our calculations indicate that many more phosphides might exhibit low thermal conductivity as well as interesting band structure characteristics for TE applications and are interesting candidates for further exploration by theorists and experimentalists alike.


3.5. Experimental Study of c-NiP$_2$

Because most studies reported in the literature focussed only on the electronic or thermal properties or are heavily doped, the cubic phase of nickel

diphosphide was synthesized in the present study to experimentally determine the intrinsic electrical and thermal transport properties on the same sample (Details about the synthesis and characterization are given in the Supplementary Information). The selection of NiP_2 was based on our aim for a simple (in this case binary) MP with excellent intrinsic properties (thereby avoiding the matter of doping for better comparison between computed and experimental properties), that would be readily accessible by solid-state synthesis and, preferably, stable in oxidative conditions for ease of handling. Furthermore, in contrast to m-NiP_2[91] the electronic or thermal properties of c-NiP_2 have not been reported.

3.4.1. Electronic Properties

Our DFT-PBE calculation predicted that the c-NiP_2 is more stable (13 meV/atom) than m-NiP_2 ($T = 0$ K; $P = 0$). The PBE exchange correlation functional indicates bang gap energies of 0 eV and 0.53 eV for c-NiP_2 and m-NiP_2, respectively (Figure S1), but the values are 0.13 eV and 1.15 eV, respectively, when using the more accurate HSE functional. Both functionals indicate high PFs for p-and n-type (Table S1 and S2), with the HSE results showing even higher maximum PFs. Furthermore, m-NiP_2 has a highly anisotropic layered structure with pseudo-planes of Ni_2P_4 along the c-axis connected through Ni-Ni bonds, leading to highest PFs along the b-axis (5.7/6.7 mW m^{-1} K^{-2} for p-/n-type, respectively) (Table S3). The pyrite c-NiP_2 structure, on the other hand, is isotropic with three degenerate valleys in the conduction band and twelve valleys in the valence band (Figure 2 (a) and 6 (a)) contributing to the electrical properties resulting in high p-and n-type PFs (3.8/2.8 mW m^{-1} K^{-2}, respectively). However, κ_e is significant, which limits the TE performance.
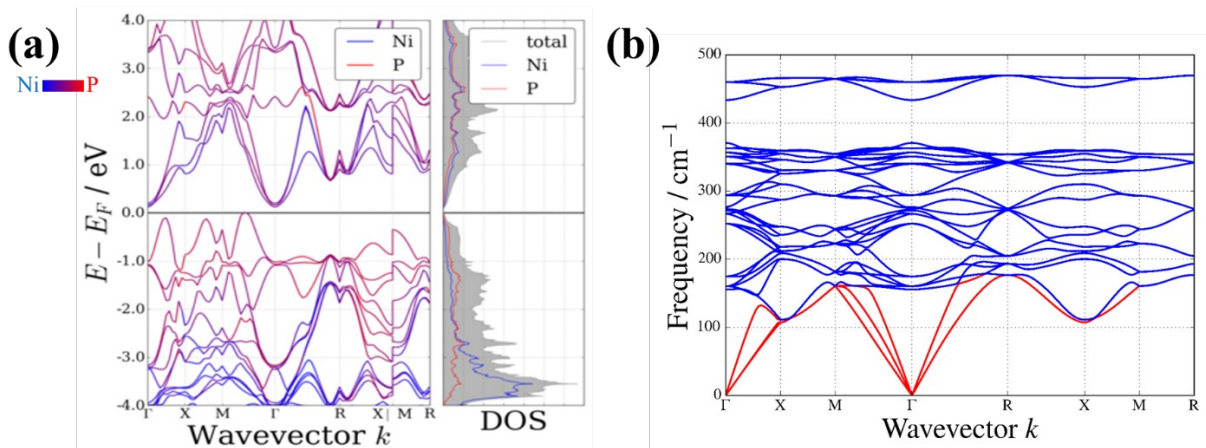
Figure 6: Computed (a) HSE-electronic and (b) PBE-phonon dispersion curve of c-NiP_2. The electronic structure in (a) shows good p- and n-PFs, while in (b) the optical phonons (blue) have relatively low frequencies and suppress the acoustic phonons (red).

While the electronic properties of single-crystalline m-NiP$_2$ were previously measured by Odile $et\ al.$ showing a high resistivity and Seebeck coefficient (Table 1),[91] the electronic properties of c-NiP$_2$ were unknown. In the present study, the transport properties of c-NiP$_2$ were determined from 2 K to 725 K (experimental data are listed in Tables S13, S14, and S15 in Supplementary Information). The low-temperature transport properties were measured with the thermal transport option using a steady-state method in a Quantum Design PPMS. This has the advantage of measuring the transport properties simultaneously. However, the contact resistance between the sample and the contacts can influence ρ and thermal conductivity, in particular if the values are low. While the low-temperature ρ was measured with a two-probe method (2Ω), the high-temperature ρ was determined by the van der Pauw method. The latter method is preferable to determine low ρ because the measurement avoids contributions from the contact resistance. At room temperature, a difference in resistance of 10 mΩ (resistivity difference of 24 mΩ cm) was observed between the low and high temperature measurements and attributed to the contact resistance. The low-temperature electrical resistivity measurements were empirically adjusted to the van der Pauw measurement at $T = 312$ K, assuming the contact resistance to be independent of temperature. The resistivity decreases with increasing temperature over the entire temperature range, indicating intrinsic semiconducting behavior (Figure 7 (b) and S7 (a)). From the curved conduction bands at the band gap a high mobility, μ, is possible due to their low effective mass (Figure 6 (a)). However, μ is reduced due to the nanoporous structure and the small grains resulting in nearly T-independent behavior (Figure 7 (a)). Another reason for the low mobility can be the high carrier concentration ($\sim 1.7 \cdot 10^{21}$ cm^{-3}) which can be related to the low band gap energy (~ 0.13 eV with HSE) leading to an enhanced ionized impurity scattering. Furthermore, we also have calculated the resistivity using the AMSET model which takes into account various scattering mechanisms, such as optical phonon scattering and ionized impurity scattering rather than assuming a constant relaxation time.[94] Taking these scattering mechanisms into account we calculated resistivity in the range of 0.60-0.74 m$\Omega \bullet$cm, still considerably lower than the measured conductivity, reinforcing the hypothesis that the low measured mobility is due to nanosized pores and scattering from small grains.

Because of the low effective mass, small E_g, and the high n ($>10^{21}$ cm^{-3}), $|S|$ is relatively low (Figure 7 (c) and S7 (b)) for c-NiP$_2$, as is the case for most small band gap TEs.[95] The magnitude of S increases to 57 μV K^{-1} from 2 K to 600 K; above 600 K the excited minority carriers reduce $|S|$. The negative value of S indicates that electrons are the dominant charge carriers, consistent with the negative Hall coefficient and the monoclinic phase (Table 1). While the magnitude of the Seebeck coefficient at 650 K is only slightly

lower than at 600 K, the magnitude drops at 700 K, most likely due to a dramatic increase in carrier concentration (Figure 7 (a)). The Goldsmid-Sharp band gap energy ($E_{g,GS}=2|S|_{max}T_{max}=0.07$ eV) is lower than the HSE band gap energy ($E_{g,HSE} = 0.13$ eV). However, the Goldsmid-Sharp equation is not valid for narrow band gaps ($E_g \leq 6\ k_B T$).[96]

The experimental electrical properties of the monoclinic and cubic phase of NiP_2 are compared to the calculated values from the Boltzmann transport equations using a constant relaxation time approach and a constant (experimentally determined) doping level, $n = 1.7 \pm 0.2 \cdot 10^{21}$ cm^{-3} (see Figure 7). While the computed electrical resistivity of both phases is dramatically underestimated, the experimental Seebeck coefficient is similar to the computation (Table 1). The electrical resistivity in c-NiP_2 is more than one order of magnitude underestimated than m-NiP_2. The larger discrepancy between experiments and computation in c-NiP_2 is most likely a result of the microstructure effects (nanosized pores and small grain size; see Figure S5 (b)). This is consistent with the mobility results which are low and nearly temperature-independent from 300 K to 650 K (Figure 7 (a)). Furthermore, the higher carrier concentration results in an increase in ionized impurity scattering and hence, limits the relaxation time. However, although the monoclinic phase is single-crystalline and the carrier concentration is low, it exhibits about four times higher resistivity than our computed values at room temperature (Table 1) and thus, the intrinsic relaxation time of NiP_2 is most likely shorter than 10^{-14} s. The overestimation of the relaxation time is not consistent within the metal phosphites as several compounds have a lower experimental resistivity than our calculated values and thus, further investigations of the intrinsic relaxation time in materials are recommended.

In contrast to ρ, the computed S agrees well with experiments (Figure 7 (c)). In particular, the computed S from the HSE band structure are within the uncertainty of the experimental results up to approximately 600 K. The discrepancy at high temperatures might be the result of increased carrier concentration and/or differences in band gap.
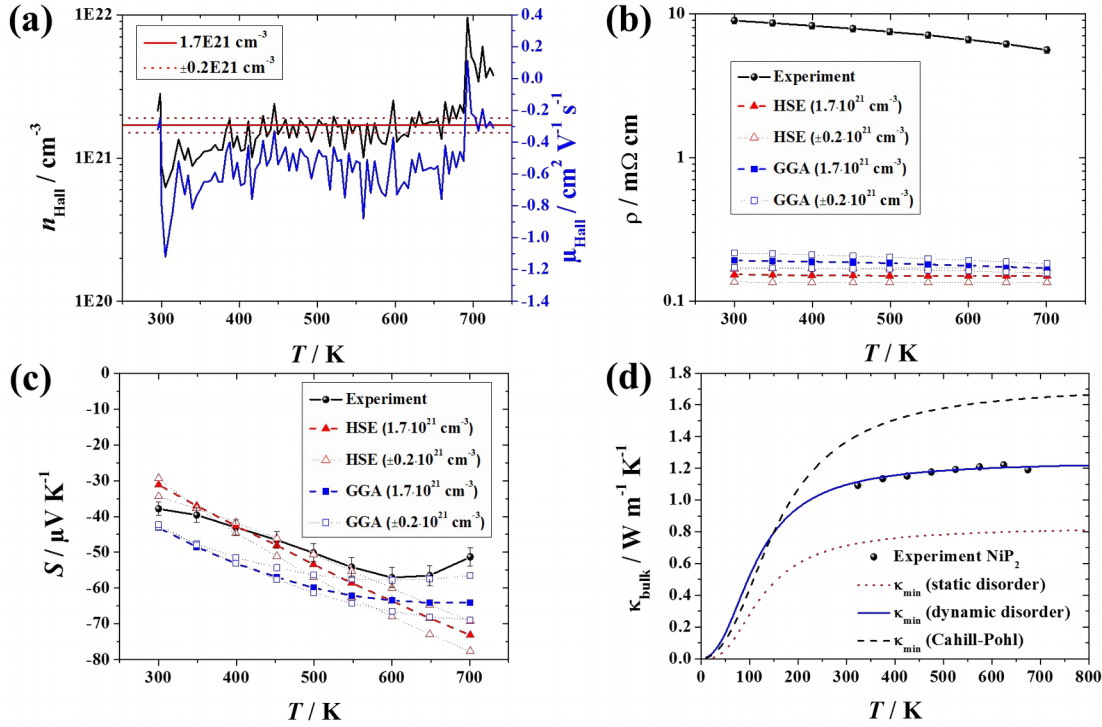
Figure 7: (a) Experimental Hall carrier concentration, n_{Hall}, and Hall mobility, μ_{Hall}, of *c*-NiP$_2$. Red lines indicate the carrier concentration used for the computational study. Comparisons of the computed and experimental results for (b) the electrical resistivity, ρ, (c) Seebeck coefficient, *S*, and (d) the phononic contribution of the thermal conductivity of a fully dense solid, κ_{bulk} show that *S* and κ_{bulk} from the computations agree remarkably well with the experiments (especially given the set relaxation time of 10^{-14} s in the calculations) while the computed ρ is lower than experiments. Most likely the nanostructure (Figure S5) and high carrier concentration cause the experimental resistivity to be higher than calculated.

3.4.3. Thermal Properties

In addition to the electronic band structure, the phonon dispersion curve of *c*-NiP$_2$ also was computed, revealing κ_{min} ranging from 0.8 to 1.4 W m^{-1} K^{-1} (Figure 6 (b); Table S5). Potential reasons for the low computed κ_{min} could be the voids in the crystal structure due to distorted pentagonal channels and/or low-frequency phonons reducing κ_p due to avoided crossings. Splitting of the optical phonons assigned to the weak Ni-P bonds (force constant 4.63 eV/Å^2) and strong P-P bond stretching modes (10.28 eV/Å^2) was observed (Figure 6 (b)). This is consistent with the Ni-P (2.29 Å) and P-P (2.19 Å) bond lengths, which are both smaller than the sum of the covalent radii (P: 1.10 Å; Ni: 1.23 Å),[97] indicating, together with the small charge transfer

between Ni and P, a weak interaction and low-frequency modes. These modes could lower both the frequency of the acoustic phonons and κ_{min}.

The phonon dispersion curve calculations are consistent with the experimental heat capacity results (see Tables S11 and S12 in Supplementary Information for data), when the electronic contribution of the heat capacity, $C_{p,el}$, is added to the computed heat capacity (Figure 8 (a)). The electronic contribution of the heat capacity was acquired by fitting of the experimental heat capacity at low temperatures with a Sommerfeld constant of 100 mJ mol^{-1} K^{-2} (Figure 8 (b)). Although the low-temperature experimental heat capacity data suggest that the low-frequency optical modes and acoustic modes of the calculated phonon dispersion curves should shift to lower frequencies, the computed heat capacity agrees well with the experimental results above 100 K when the electronic contribution is added (Figure 8 (a)). However, note that the heat capacity was computed with a harmonic approach and anharmonicity can play a significant role at high temperatures. The calculated Grüneisen parameter (γ) from 20 K to 400 K indicates a relatively low and nearly temperature-independent anharmonicity ($\gamma \sim 1$). This is typical for structures containing both tetrahedral and octahedral local environments[81] and agrees with the computed Grüneisen parameter using the equation reported by Miller *et al.*[37] Most tetrahedral structures (*e.g.,* ZnS or Si) have a Grüneisen parameter value of approximately 0.5 to 0.7 while binary system with octahedral environments have values between 1.5 to 2.[81] Furthermore, the Grüneisen parameter in *c*-NiP$_2$ is slightly higher than for GaP.[81] However, this cannot explain the low κ_{min}.
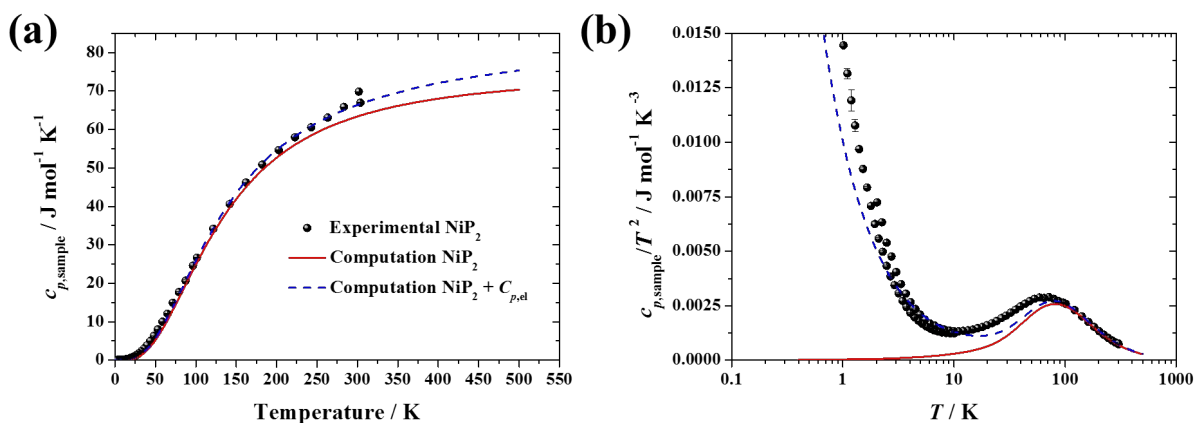
Figure 8: (a) Heat capacity of *c*-NiP$_2$. Experimental results agree with the calculated heat capacity from PBE-GGA calculations when the electronic contribution of the heat capacity, $C_{p,el}$, is included. (b) C_p/T^2 vs T indicates low frequency optical modes. A discrepancy between the calculated and experimental heat capacity appears at low temperatures.

The experimental thermal conductivity at high temperature was determined from the measured thermal diffusivity, the mass density, and the computed heat capacity including the electronic contribution of the heat capacity, whereas the low-temperature thermal conductivity was measured directly. The thermal conductivities from low- and high-temperature measurements (Figure S7 (c)) are different at room temperature but within their uncertainties (5% for low-temperature and 15% for high-temperature thermal conductivity). It is important to note that the thermal conductivity measurements at high temperatures have a higher uncertainty than the low temperature results due to the additive uncertainties of the mass density, thermal diffusivity, and heat capacity. However, for the low-temperature thermal conductivity measurements in the PPMS an emissivity of one was assumed and this assumption for blackbody radiation can lead to a large error, especially at high temperatures ($T > 300$ K) due to the T^4 relationship.

The phononic (*i.e.,* experimental minus electronic) contribution of the thermal conductivity of c-NiP$_2$ was compared to the minimum thermal conductivity models (described above). The electronic contribution of the thermal conductivity was calculated using the single parabolic band (SPB) model. [96] The resulting phononic contribution of the thermal conductivity, κ_p, was corrected to zero porosity using

$$\kappa_{bulk} = \frac{\kappa_p}{1 - \dfrac{4\Phi}{3}} \tag{3}$$

where $\Phi = 0.18$ is the porosity using the density of the pellet (4.04 g cm^{-3}) and the theoretical density of c-NiP$_2$ (4.90 g cm^{-3}).[98] While the electronic contribution of the thermal conductivity of c-NiP$_2$ increases with temperature, κ_{bulk} has a glassy behavior where the thermal conductivity increases to 1.2 W m^{-1} K^{-1}, followed by a temperature-independent plateau.

κ_{bulk} determined from the experimental thermal conductivity is below the minimum thermal conductivity using the Cahill and Pohl model and agrees well with the minimum thermal conductivity using an average phonon mean speed and a frequency-dependent phonon mean free path (Figure 7 (d)), as also observed for Zn$_3$P$_2$ (Figure S3). In both cases, the phonon mean free path is most likely limited by the nano-sized grains which scatter the acoustic phonons. κ_{SE} is not shown in the figure as it is more than one order of magnitude higher at 300 K than the experimental value.

The transport properties are summarized by the TE figure of merit which increases with temperature up to 0.03 at 650 K (Figure S7 (d)), which is in the range of the predicted $zT_{calc}(\kappa_{min})$ ~0.17 and $zT_{calc}(\kappa_{SE})$ ~0.11 using the HSE band structures. From the SPB model, it was observed that a slight

reduction of the carrier concentration might increase zT to 0.04. Although κ_{bulk} is lower than κ_{min} and κ_{SE}, overestimating the TE performance, the underestimated ρ leads to an overestimation of zT_{calc} which is most likely due to the overestimated fixed relaxation time. A better approximation for the relaxation time would enhance the prediction of ρ and hence, zT. Another potential approach to increase efficiency is reduction of porosity by further consolidation of the sample. A denser sample would enhance the mobility and most likely increase the figure of merit.

4. Conclusions

From a high-throughput screening of 48,000 compounds[23], metal phosphides were revealed as a potential class of high-performance thermoelectric materials. Electronic and thermal properties were computed in which several MP compounds were discussed that could possibly possess moderate or high thermoelectric efficiency. In particular, XYP compounds show high n-type PF due to multi-valley degeneracy and low κ_p which is higher than the predicted thermoelectric performance for the current best TE materials (*i.e.* PbTe and Bi_2Te_3) within the set of approximations and assumptions (*e.g.*, constant relaxation time and an estimated thermal conductivity) employed. Enhanced electronic properties also were found for GaP. However, due to the high predicted thermal conductivity using a semi-empirical approach the TE performance of GaP is limited. The computation was supported by experimental studies indicating good agreement between computed and experimental transport properties. In particular, three MPs (IrP_2, CuP_2, and Cd_3P_2) exhibit enhanced electrical properties and/or low thermal conductivity. of c-NiP_2 which demonstrates good electronic transport and thermal properties. While the Seebeck coefficient and thermal conductivity agree well with the computed data, the electrical resistivity was severely underestimated computationally (Figure 7 (b)), most likely due to the nanoporous structure of the consolidated pellet and the universal constant relaxation time on which experiments were performed and not included in the models. Further studies of other MP compounds are in progress to investigate the effect of densification on electron transport and its influence on zT.

[1]   G. J. Snyder, E. S. Toberer, *Nature Mater.* **2008**, *7*, 105-114.
[2]   Y. Pei, H. Wang, G. J. Snyder, *Adv. Mater.* **2012**, *24*, 6125-6135.
[3]   K. Biswas, J. He, I. D. Blum, C.-I Wu, T. P. Hogan, D. N. Seidman, V. P. Dravid, M. G. Kanatzidis, *Nature*
      2012, *489*, 414-418.
[4]   D. M. Rowe, Thermoelectrics Handbook : Macro to Nano, CRC ; London : Taylor & Francis, Boca Raton, Fla.,
      2006.
[5]   D. G. Cahill, R. O. Pohl, *Ann. Rev. Phys. Chem.* **1988**, *39*, 93-121.
[6]   D.G. Cahill, S. K. Watson, R. O. Pohl, *Phys. Rev. B* **1992**, *46*, 6133-6140.
[7]   U. Aydemir, C. Candolfi, A. Ormeci, Y. Oztan, M. Baitinger, N. Oeschler, F. Steglich, Y. Grin, *Phys. Rev. B*
       2011, *84*, 043715.
[8]   A.D. Ritchie, M.B. Johnson, J.F. Niven, M. Beekman, G.S. Nolas, J. Gryko, M.A. White, *J. Phys.: Condens.*
       Matter **2013**, *25*, 435401.
[9] S. M. Kauzlarich, S. R. Brown, G. J. Snyder*, Dalton Trans*. **2007**, 2099-2107.
[10] S. Ohno, U. Aydemir, M. Amsler, J.-H. Pöhls, S. Chanakian, A. Zevalkink, M. Wood, M.A. White, S.K. Bux, C. Wolverton, G. J. Snyder, *Adv. Funct. Mater.* **2017**, *27*, 1606361.
[11] X. Shi, J. Yang, J. R. Salvador, M. F. Chi, J. Y. Cho, H. Wang, S. Q. Bai, J. H. Yang, W. Q. Zhang, L. D. Chen, *J. Am. Chem. Soc*. **2011**, *133*, 7837-7846.
[12]   [ ] H. Chen, Q. Hao, O. Zivkovic, G. Hautier, L.-S. Du, Y. Tang, Y.-Y. Hu, X. Ma, C. P. Grey, G. Ceder, *Chem. Mater.* **2013**, *25*, 2777-2786.
[13]   [] Q. Yan, G. Li, P. F. Newhous, J. Yu, K. A. Persson, J. M. Gregoire, J. B. Neaton, *Adv. Energy Mater.* **2015**, *5*, 1401840.
[14]   [] J. M. Cole, K.S. Low, H. Ozoe, P. Stathi, C. Kitamura, H. Kurata, P. Rudolf, T. Kawase, *Phys. Chem. Chem. Phys.* **2014**, *16*, 26684-26690.
[15]   [] J. Carrete, N. Mingo, S. Wang, S. Curtarolo, *Adv. Funct. Mater.* **2014***, 24*, 7427–7432.
[16]   [] J. He, M. Amsler, Y. Xia, S. S. Naghavi, V. I. Hegde, S. Hao, S. Goedecker, V. Ozoliņš, Chris Wolverton, *Phys. Rev. Lett.* **2016**, *117*, 046602.
[17]   [] L. Bjerg, G. K. H. Madsen, B. B. Iversen, *Chem. Materials* **2011**, *23*, 3907–3914.
[18] [] G. K. H. Madsen, *J. Amer. Chem. Soc.* **2006**, *128*, 12141-12146.
[19]   [] I. Opahle, A. Parma, E. J. McEniry, R.Drautz, G. K. H. Madsen, *New Journal Phys.* **2013**, *15*, 105010.
[20]   [] P. Gorai, E. S. Toberer, V. Stevanovic. *Phys. Chem. Chem. Phys.* **2016**, *18*, 31777-31786.
[21]   [] H. Zhu, G. Hautier, U. Aydemir, Z.M. Gibbs, G. Li, S. Bajaj, J.-H. Pöhls, D. Broberg, W.Chen, A. Jain, M. A. White, M. Asta, G. J. Snyder, K. Persson, G. Ceder, *J. Mater. Chem. C* **2015***, 3*, 10554-10565.
[22]   [] U. Aydemir, J.-H. Pöhls, H. Zhu, G. Hautier, S. Bajaj, Z. M. Gibbs, W. Chen, G. Li, S. Ohno, D. Broberg, S. D. Kang, M. Asta, G. Ceder, M. A. White, K. Persson, A. Jain, G. J. Snyder, *J. Mater. Chem. A* **2016**, *4*, 2461-2472.
[23]   [] W. Chen, J.-H. Pöhls, G. Hautier, D. Broberg, S. Bajaj, U. Aydemir, Z. M. Gibbs, H. Zhu, M. Asta, G. J. Snyder, B. Meredig, M. A. White, K. Persson, A. Jain, *J. Mater. Chem. C* **2016**, *4*, 4414-4426 .
[24] F. Ricci, W. Chen, U. Aydemir, G. J. Snyder, G.-M. Rignanese, A. Jain, G. Hautier, *Sci. Data* **2017**, *4*, 170085.
[25]   [] Y. Kumashiro, M. Hirabayashi, T. Koshiro, Y. Okada, *J. Less-Common Metals* **1988**, *143*, 159–165.
[26] [] I. Kudman, E. F. Steigmeier, *Phys. Rev.* **1964**, *133*, A1665-A1667.
[27]   [] J. V. Zaikina, K. A. Kovnir, A. N. Sobolev, I. A. Presniakov, V. G. Kytin, V. A. Kulbachinskii, A. V. Olenev, O. I. Lebedev, G, Van Tendeloo, E. V. Dikarev, A. V. Shevelkov, *Chem. Mater.* **2008**, *20*, 2476–2483.
[28] A. Watcharapasorn, R. C. DeMattei, R. S. Feigelson, T. Caillat, A. Borshchevsky, G. J. Snyder, J.-P. Fleurial, J. *Appl. Phys.* **1999**, *86*, 6213-6217.
[29]   [] A. D. Martinez, E. L. Warren, P. Gorai, K. A. Borup, D. Kuciauskas, P. C. Dippo, B. R. Ortiz, R. T. Macaluso, S. D. Nguyen, A. L. Greenaway, S. W. Boettcher, A. G. Norman, V. Stevanovic, E. S. Toberer, A. C. Tamboli, *Energy Environ. Sci.* **2016**, *9*, 1031-1041.
[30] J. Zhang, H. J. Liu, L. Cheng, J. Wei, J. H. Liang, D. D. Fan, P. H. Jiang, L. Sun, J. Shi, *J. Mater. Chem. C* **2016**, *4*, 991-998.
[31]   [] T. Yi, G. Zhang, N. Tsujii, J.-P. Fleurial, A. Zevalkink, G. J. Snyder, N. Grønbech-Jensen, S. M. Kauzlarich, *Inorg. Chem.* **2013**, *52*, 3787−3794.
[32] J.-A. Dolyniuk, J. Wang, K. Lee, K. Kovnir, *Chem. Mater.* **2015**, *27*, 4476-4484.

[33] J. V. Zaikina, T. Mori, K. Kovnir, D. Teschner, A. Senyshyn, U. Schwarz, Y. Grin, A. V. Shevelkov, *Chem. Eur. J.* **2010**, *16*, 12582-12589.

[34] J. Nuss, U. Wedig, W. Xie, P. Yordanov, J. Bruin, R. Hübner, A. Weidenkaff, H. Takagi, *Chem. Mater.* **2017**, *accepted*.

[35] J.-H. Pöhls, M. B. Johnson, M. A. White, *Phys. Chem. Chem. Phys.* **2016**, *18*, 1185-1190.

[36] S. A. Miller, P. Gorai, B. R. Ortiz, A. Goyal, D. Gao, S. A. Barnett, T. O. Mason, G. J. Snyder, Q. Lv, V. Stevanović, E. S. Toberer, *Chem. Mater..* **2017**, *29*, 2494-2501.

[37] V. S. Babu, P. R. Vaya, J. Sobhanadri, *J. Appl. Phys.* **1988**, *64*, 1922-1926.

[38] W.D. Thompson, R. Vaddi, B.E. White Jr., *J. Alloys Comp.* **2016**, *687*, 813-820.

[39] G. Kresse, J. Furthmüller, *Phys. Rev. B* **1996**, *54*, 11169–11186.

[40] J. P. Perdew, K. Burke, M. Ernzerhof, *Phys. Rev. Lett.* **1996**, *77*, 3865–3868.

[41] G. Kresse, D. Joubert, *Phys. Rev. B* **1999**, *59*, 1758–1775.

[42] J. Heyd, G. E. Scuseria, M. Ernzerhof, *J. Chem. Phys.* **2003**, *118*, 8207–8215.

[43] J. Paier, M. Marsman, K. Hummer, G. Kresse, I. C. Gerber, J. G. Angyán, *J. Chem. Phys.* **2006**, *124*, 154709.

[44] G. K. H. Madsen, D. J. Singh, *Comput. Phys. Commun.* **2006**, *175*, 67–71.

[45] S. P. Ong, W. D. Richards, A. Jain, G. Hautier, M. Kocher, S. Cholia, D. Gunter, V. L. Chevrier, K. A. Persson, G. Ceder, *Comput. Mater. Sci.* **2013**, *68*, 314–319.

[46] A. Jain, S. P. Ong, W. Chen, B. Medasani, X. Qu, M. Kocher, M. Brafman, G. Petretto, G.-M. Rignanese, G. Hautier, D. Gunter, K. A. Persson, *Concurrency Computat.: Pract. Exper.* **2015**, *27*, 5037–5059.

[47] K. Mathew, J. H. Montoya, A. Faghaninia, S. Dwarakanath, M. Aykol, H. Tang, I.-h. Chu, T. Smidt, B. Bocklund, M. Horton, J. Dagdelen, B. Wood, Z.-K. Liu, J. Neaton, S. P. Ong, K. Persson, A. Jain, *Comput. Mater. Sci.* **2017**, *139*, 140-152.

[48] M. de Jong, W. Chen, T. Angsten, A. Jain, R. Notestine, A. Gamst, M. Sluiter, C. K. Ande, S. Van Der Zwaag, J. J. Plata, C. Toher, S. Curtarolo, G. Ceder, K. A. Persson, M. Asta, *Sci. Data* **2015**, *2*, 150009.

[49] A. Walle, M. Asta, G. Ceder, *Calphad.* **2002**, *26*, 539-553.

[50] W. Tang, E. Sanville, G. Henkelman, *J. Phys.: Condens. Matter* **2009**, *21*, 084204.

[51] X. Gonze, B. Amadon, P.M. Anglade, J.-M. Beuken, F. Bottin, P. Boulanger, F. Bruneval, D. Caliste, R. Caracas, M. Cote, T. Deutsch, L. Genovese, Ph. Ghosez, M. Giantomassi, S. Goedecker, D. Hamann, P. Hermet, F. Jollet, G. Jomard, S. Leroux, M. Mancini, S. Mazevet, M. J. T. Oliveira, G. Onida, Y. Pouillon, T. Rangel, G.-M. Rignanese, D. Sangalli, R. Shaltaf, M. Torrent, M. J. Verstraete, G. Zérah, J. W. Zwanziger, *Comput. Phys. Commun.* **2009**, *180*, 2582-2615.

[52] X. Gonze, *Phys. Rev. B* **1997**, *55*, 10337.

[53] X. Gonze, C. Lee, *Phys. Rev. B* **1997**, *55*, 10355.

[54] C. Lee, X. Gonze, *Phys. Rev. B* **1995**, *51*, 8610.

[55] X. Gonze, F. Jollet, F. Abreu Araujo, D. Adams, B. Amadon, T. Applencourt, C. Audouze, J.-M. Beuken, J. Bieder, A. Bokhanchuk, E. Bousquet, F. Bruneval, D. Caliste, M. Côté, F. Dahm, F. Da Pieve, M. Delaveau, M. Di Gennaro, B. Dorado, C. Espejo, G. Geneste, L. Genovese, A. Gerossier, M. Giantomassi, Y. Gillet, D. R. Hamann, L. He, G. Jomard, J. Laflamme Janssen, S. Le Roux, A. Levitt, A. Lherbier, F. Liu, I. Lukačević, A. Martin, C. Martins, M. J. T. Oliveira, S. Poncé, Y. Pouillon, T. Rangel, G.-M. Rignanese, A. H. Romero, B. Rousseau, O. Rubel, A. A. Shukri, M. Stankovski, M. Torrent, M. J. Van Setten, B. Van Troeye, M. J. Verstraete, D. Waroquiers, J. Wiktor, B. Xu, A. Zhou, J. W. Zwanziger, *Comput. Phys. Commun.* **2016**, *205*, 106-131.

[56] P. Nath, J. J. Plata, D. Usanmaz, C. Toher, M. Fornari, M. Buongiorno Nardelli, S. Curtarolo, *Scr. Mater.* **2017**, *129*, 88-93.

[57] L. Bjerg, B. B. Iversen, G. K. H. Madsen, *Phys. Rev. B* **2014**, *89*, 024304.

[58] B. Hunter (1998) "Rietica - A visual Rietveld program", International Union of Crystallography Commission on Powder Diffraction Newsletter No. 20, (Summer) http://www.rietica.org.

[59] C. A. Kennedy, M. Stancescu, R. A. Marriott, M. A. White, *Cryogenics* **2007**, *47*, 107–112.

[60] O. Maldonado, *Cryogenics* **1992**, *32*, 908-912.

[61] C. A. Kennedy and M. A. White, *Solid State Commun.* **2005**, 134, 271-276.

[62] K. A. Borup, E. S. Toberer, L. D. Zoltan, G. Nakatsukasa, M. Errico, J. P. Fleurial, B. B. Iversen, G. J. Snyder, *Rev. Sci. Instrum.* **2002,** *83*, 123902.

[63] S. Iwanaga, E. S. Toberer, A. LaLonde, G. J. Snyder, *Rev. Sci. Instru.* **2011**, *82*, 063905.

[64] A. Jain, S.P. Ong, G. Hautier, W. Chen, W.D. Richards, S. Dacek, S. Cholia, D. Gunter, D. Skinner, G. Ceder, K.A. Persson, *APL Materials* **2013**, *1*, 011002.

[65] J. B. Varley, A. Miglio, V.-A. Ha, M. J. van Setten, G.-M. Rignanese, Geoffroy Hautier, *Chem. Mater.* **2017**, *29*, 2568-2573.

[66] H. Wang, Y. Pei, A. LaLonde, G. J. Snyder, in *Thermoelectric Nanomaterials*, ed. K. Koumoto and T. Mori, Springer, Berlin Heidelberg, 2013, vol. 182, ch. 1, pp. 3–32.

[67] L. J. Sham, M. Schlüter, *Phys. Rev. Lett.* **1983**, *51*, 1888–1891.

[68] J. P. Perdew, M. Levy, J. P. Perdew, *Phys. Rev. Lett.* **1983**, *51*, 1884–1887.

[69] M. Chan, G. Ceder, *Phys. Rev. Lett.* **2010**, *105*, 196403.

[70] W. Setyawan, R. M. Gaume, S. Lam, R. S. Feigelson, S. Curtarolo, *ACS Comb. Sci.* **2011**, *13*, 382–390.

[71] W. Weber, *Phys. Rev. B* **1977**, *15*, 4789-4803.

[72] D. Strauch, B. Dorner, *J. Phys.: Condens. Matter* **1990**, *2*, 1457-1474.

[73] S. Lee, K. Esfarjani, T. Luo, J. Zhou, Z. Tian, G. Chen, *Nat. Commun.* **2014**, *5*, 3525.

[74] A. Jain, A. J. H. McGaughey, *Sci. Rep.* **2015**, *5*, 8501

[75] D. O. Lindroth, P. Erhart, *Phys. Rev. B* **2016**, *94*, 115205.

[76] A. Togo, I. Tanaka, *Scr. Mater.* **2015**, *108*, 1-5.

[77] A. Seko, A. Togo, H. Hayashi, K. Tsuda, L. Chaput, Isao Tanaka, *Phys. Rev. Lett.* **2015**, *115*, 205901.

[78] A. van Roekeghem, J. Carrete, C. Oses, S. Curtarolo, N. Mingo, *Phys. Rev. X* **2016**, *6*, 041061.

[79] C. Chiritescu, D. G. Cahill, N. Nguyen, D. Johnson, A. Bodapati, P. Keblinski, P. Zschack, *Science* **2007**, *315*, 351-353.

[80] W. G. Zeier, A. Zevalkink, Z. M. Gibbs, G. Hautier, M. G. Kanatzidis, G. J. Snyder, *Angew. Chem. Int. Ed.* **2016**, *55*, 6826 –684.

[81] G.A. Slack, *J. Phys .Chem. Solids* **1973**, *34*, 321–335.

[82] E.F. Steigmeier, I. Kudman, *Phys. Rev.* **1963**, *132*, 508–512.

[83] S. A. Aliev, A. Ya. Nashelskii, S. S. Shalyt, *Sov. Phys. Solid State* (English Transl.) **1965**, *7*, 1287; *Fiz. Tverd. Tela* **1965**, *7*, 1590.

[84] Y. Kumashiro, M. Hirabayashi, T. Koshiro and Y. Okada, *J. Less-Common Met.* **1988**, *143*, 159-165.

[85] S. Yugo. T. Sato. T. Kimura, *Appl. Phys. Lett.* **1985**, *46*, 842-844.

[86] I. S. Gorban, G. A. Grishchenko, A. P. Sakalas, A. S. Sodeika, I. I. Tychina, A. K. Tkachenko, *Phys. Stat. Sol. (a)* **1978**, *48*, 329-334.

[87] K. Masumoto, S. Isomura, K. Sasaki, *Phys. Stat. Sol. (a)* **1971**, *6*, 515–523.

[88] W.D. Thompson, Rajesh Vaddi, B.E. White Jr., *J. Alloys Compd*. **2016**, *687*, 813-820.

[89] W. Zdanowicz and A. Wojakowski, *Phys. Stat. Sol.* **1965**, *8*, 569-575.

[90] R. Kaner, C. A. Castro, R. P. Gruska, A. Wold, *Mat. Res. Bult.* **1977**, *12*, 1143-1147.

[91] J. P. Odile, S. Soled, C. A. Castro, A. Wold, *Inorg. Chem*. **1978**, *17*, 283-286.

[92] A. H. Reshak, S. Auluck, *Comput. Mater. Sci.* **2015**, *96*, 90-95.

[93] O. Madelung, U. Rössler, M. Schulz (ed.), Indium phosphide (InP), electrical and thermal conductivity, carrier concentrations; Landolt-Börnstein - Group III Condensed Matter 41A1β (Group IV Elements, IV-IV and III-V Compounds. Part b - Electronic, Transport, Optical and Other Properties), Springer-Verlag, Berlin Heidelberg, 2002.

[94] A. Faghaninia, C. S. Lo, J. W. Ager, *Phys. Rev. B* **2015**, *91*, 235123.

[95] A. F. May, E. S. Toberer, G. J. Snyder, *J. Appl. Phys.* **2009**, *106*, 013706.

[96] Z. M. Gibbs, H.-S. Kim, H. Wang, G. J. Snyder, *Appl. Phys. Lett.* **2015**, *106*, 022112.

[97] F. Gillot, S. Boyanov, L. Dupont, M.-L. Doublet, M. Morcrette, L. Monconduit, J.-M. Tarascon, *Chem. Mater.* **2005**, *17*, 6327-6337.

[98] P. G. Klemens, *High Temp. - High Pressures* **1991**, *23*, 241.